Polymers with Cavities Tuned for Fast Selective Transport of Small Molecules and Ions

Ho Bum Park, *et al.*

Science **318**, 254 (2007);
DOI: 10.1126/science.1146744

Science (print ISSN 0036-8075; online ISSN 1095-9203) is published weekly, except the last week in December, by the American Association for the Advancement of Science, 1200 New York Avenue NW, Washington, DC 20005.

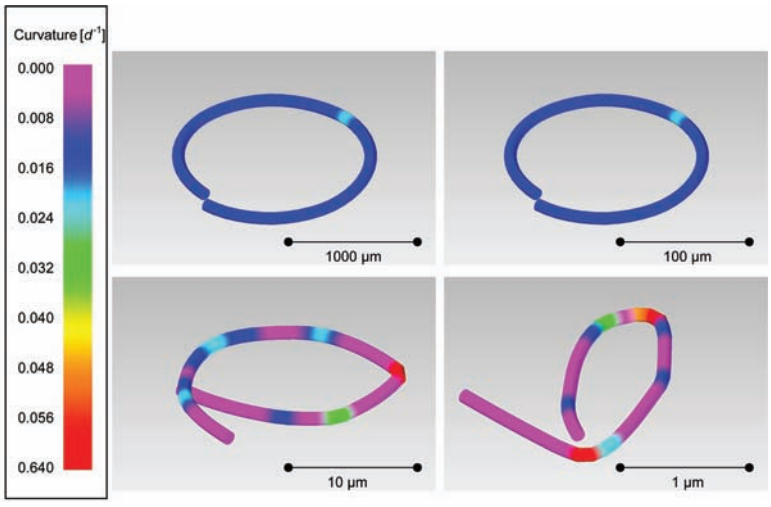

Fig. 4. Shapes of rods (aspect ratio 1:50) after simulated bending; rod thickness t from top left to bottom right: $t = 100$ μm, $t = 10$ μm, $t = 1$ μm, $t = 0.1$ μm; $b = 2.8 \times 10^{-10}$ m, $\Theta = E/1000$; the color code indicates the local bending angle over a segment of length t. In the last rod, the maximum avalanche size occurring in the simulations falls below the intrinsic cut-off of the distribution.

ries hinder avalanche propagation (fig. S4), and thus the size of strain bursts is reduced by a factor of $(\xi/L)^2$, where ξ is the grain size [see (*19*) for a more detailed discussion]. Accordingly, formability may be ensured even on the submicrometer scale if a correspondingly small grain size can be maintained throughout the processing.

Our results demonstrate the universality of avalanche behavior in plasticity and elucidate the crossover between intermittent and smooth plastic flow. That avalanche strains decrease in inverse proportion to sample size explains why it is difficult to observe strain bursts in macroscopic samples. In AE measurements, by contrast, the acoustic energy is recorded. The acoustic energy release during a dislocation avalanche may be assumed to be proportional to the dissipated energy e, which is related to the strain s by $e \approx \sigma s V$, where σ is the stress and V is the volume. Hence, the cutoff of the AE energy distribution is expected to increase with sample size as $e_0 \propto L^2$. This explains why acoustic emission avalanches are observed in macroscopic single crystals, whereas strain avalanches are not.

The picture that emerges from our analysis indicates that, even though the phenomenology of plastic deformation changes markedly with decreasing sample size, the fundamental physical processes are the same in macroscopic and micrometer-scale specimens. Dislocation avalanches on all scales arise from the most basic features of dislocation motion and can be described by a generic statistical distribution. In single crystals, the largest dislocation avalanches extend across an entire cross section of the specimen: Their extension is limited only by the sample size, and the stochastic nature of their occurrence may make it impossible to control the shapes resulting from a deformation process. In polycrystals, by contrast, dislocation avalanches are limited by grain boundaries. This may lead to an appreciable smoothing of deformation and improve the controllability of deformation processes.

References and Notes

1. M. D. Uchic, D. M. Dimiduk, J. N. Florando, W. D. Nix, *Science* **305**, 986 (2004).
2. D. M. Dimiduk, C. Woodward, R. LeSar, M. D. Uchic, *Science* **312**, 1188 (2006).
3. M. C. Miguel, A. Vespignani, S. Zapperi, J. Weiss, J. R. Grasso, *Nature* **410**, 667 (2001).
4. J. Weiss, J. R. Grasso, *J. Phys. Chem. B* **101**, 6113 (1997).
5. J. Weiss, F. Lahaie, J. R. Grasso, *J. Geophys. Res.* **105**, 433 (2000).
6. J. Weiss, D. Marsan, *Science* **299**, 89 (2003).
7. T. Richeton, J. Weiss, F. Louchet, *Nat. Mater.* **4**, 465 (2005).
8. T. Richeton, P. Dobron, F. Chmelik, J. Weiss, F. Louchet, *Mater. Sci. Eng. A* **424**, 190 (2006).
9. J. Schwerdtfeger *et al.*, *J. Stat. Mech.* L04001 (2007).
10. L. P. Kubin, C. Fressengeas, G. Ananthakrishna, in *Dislocations in Solids*, F. R. N. Nabarro, M. S. Duesbery, Eds. (North-Holland, Amsterdam, 2002), vol. 11, p. 101.
11. J. P. Sethna, K. A. Dahmen, C. R. Myers, *Nature* **410**, 242 (2001).
12. G. Durin, S. Zapperi, in *The Science of Hysteresis*, G. Bertotti, I. Mayergoyz, Eds. (Academic Press, New York, 2005), p. 181; also available at http://arxiv.org/abs/cond-mat/0404512.
13. E. V. Colla, L. K. Chao, M. B. Weissman, *Phys. Rev. Lett.* **88**, 017601 (2002).
14. A. Petri, G. Paparo, A. Vespignani, A. Alippi, M. Costantini, *Phys. Rev. Lett.* **73**, 3423 (1994).
15. L. I. Salminen, A. I. Tolvanen, M. J. Alava, *Phys. Rev. Lett.* **89**, 185503 (2002).
16. R. F. Tinder, J. P. Trzil, *Acta Metall.* **21**, 975 (1973).
17. H. H. Potthoff, *Phys. Stat. Sol. (a)* **77**, 215 (1983).
18. H. Godon, H. H. Potthoff, H. Neuhauser, *Cryst. Lattice Defects* **19**, 373 (1984).
19. See supporting material available on *Science* Online.
20. D. Weygand, L. H. Friedman, E. van der Giessen, A. Needleman, *Model. Simul. Mater. Sci. Eng.* **10**, 437 (2002).
21. D. Weygand, P. Gumbsch, *Mat. Sci. Eng. A* **400-401**, 158 (2005).
22. M. Zaiser, P. Moretti, *J. Stat. Mech.* P08004 (2005).
23. M. Zaiser, *Adv. Phys.* **55**, 185 (2006).
24. M. Zaiser, N. Nikitas, *J. Stat. Mech.* P04013 (2007).

25. Financial support of the European Commissions Human Potential Programme SizeDepEn (contract MRTN-CT-2003-504634) and the New and Emerging Science and Technologies (NEST) Pathfinder program Triggering Instabilities in Materials and Geosystems (contract NEST-2005-PATH-COM-043386), as well as by the Engineering and Physical Science Research Council (grant EP/E029825), is gratefully acknowledged. Part of this work was performed on the PC cluster of the Department of Theoretical Physics at Eötvös University and at the High Performance Computing calculation facilities of the Rechenzentrum, University of Karlsruhe, within the HPC_DDD project. C.M. acknowledges the financial support of the Austrian Fonds zur Förderung der wissenschaftlichen Forschung (FWF) through project J2646-N13. D.W. acknowledges the financial support of the European Union project NMP3-CT-2006-016710 (NANOMESO).

Supporting Online Material

www.sciencemag.org/cgi/content/full/318/5848/251/DC1
SOM Text
Figs. S1 to S4
References

12 April 2007; accepted 17 August 2007
10.1126/science.1143719

Polymers with Cavities Tuned for Fast Selective Transport of Small Molecules and Ions

Ho Bum Park,[1,2] Chul Ho Jung,[1] Young Moo Lee,[1]* Anita J. Hill,[3] Steven J. Pas,[3] Stephen T. Mudie,[3] Elizabeth Van Wagner,[2] Benny D. Freeman,[2] David J. Cookson[4]

Within a polymer film, free-volume elements such as pores and channels typically have a wide range of sizes and topologies. This broad range of free-volume element sizes compromises a polymer's ability to perform molecular separations. We demonstrated free-volume structures in dense vitreous polymers that enable outstanding molecular and ionic transport and separation performance that surpasses the limits of conventional polymers. The unusual microstructure in these materials can be systematically tailored by thermally driven segment rearrangement. Free-volume topologies can be tailored by controlling the degree of rearrangement, flexibility of the original chain, and judicious inclusion of small templating molecules. This rational tailoring of free-volume element architecture provides a route for preparing high-performance polymers for molecular-scale separations.

Small-molecule and ion diffusion through cavities (i.e., free-volume elements) in soft organic materials is an inherently subnano- or nanoscopic phenomenon. It has important implications for membrane separation processes in chemicals production as well as energy conver-

sion and storage applications [e.g., pharmaceutical separations (*1*), organic batteries (*2*), fuel cells (*3*), and gas separation (*4*)]. Transport of small gas molecules through polymers occurs by diffusion through transient free-volume elements or cavities formed by random, thermally stimulated motion of the flexible organic chains. Unlike pore sizes and shapes in rigid microporous inorganic materials such as zeolites (*5*) and carbon molecular sieve materials (*6*), cavity sizes and shapes are not uniform in amorphous polymers. The cavity radius (r) of the most selective polymers such as polyimides, polysulfones, and polycarbonates, as measured by positron annihilation lifetime spectroscopy (PALS), is 0.3 nm or less with a broad distribution of cavity sizes, and gas permeability is rather low (*7*).

Conversely, the most permeable polymer, poly(1-trimethylsilyl-1-propyne) (PTMSP), exhibits an approximately bimodal cavity size distribution centered at around $r = 0.3$ nm and $r = 0.6$ to 0.7 nm (*8*). The high concentration of large cavities and the high connectivity among cavities results in very high permeability for a polymer, but its ability to separate small molecules (kinetic diameter <0.45 nm) is too low to be useful, and the large cavities collapse over time due to physical aging (*8*). Thus, among known polymers, free-volume element size and distribution play a key role in determining permeability and separation characteristics. However, the broad size range of free-volume elements in such materials precludes the preparation of polymers having both high permeability and high selectivity.

We demonstrate that polymers with an intermediate cavity size, a narrow cavity size distribution, and a shape reminiscent of bottlenecks connecting adjacent chambers, such as those found elegantly in nature in the form of ion channels (*9*) and aquaporins (*10*), yield both high permeability and high selectivity. Central to our approach for preparing these intermediate-sized cavities is controlled free-volume element formation through spatial rearrangement of the rigid polymer chain segments in the glassy phase. It is known that a rearrangement, such as intramolecular cyclization, in glassy polymers could lead to changes in polymer structure for gas transport (*11*). For this purpose, aromatic polymers interconnected with heterocyclic rings (e.g., benzoxazole, benzithiazole, and benzimidazole) are of interest because phenylene-heterocyclic ring units in such materials have a flat, rigid-rod structure with high–torsional energy barriers to rotation between two rings (*12*). The stiff, rigid ring units in such flat topologies pack efficiently, leaving very small penetrant-accessible free-volume elements. This tight packing is also promoted by intersegmental interactions such as charge-transfer complexes between heteroatoms containing lone electron pairs (e.g., O, S and N) (*13*). The genesis of these materials was the demand for highly thermally and chemically stable polymers. However, their application as gas separation membranes was frustrated by their lack of solubility in common solvents, which effectively prevents them from being prepared as thin membranes by solvent casting, which is the most widely practiced method for membrane preparation.

We circumvented this fabrication challenge by using postfabrication polymer-modifying reactions (*14*, *15*). Completely aromatic, insoluble, infusible polymers can be prepared from highly soluble precursors by irreversible molecular rearrangement at about 350° to 450°C for aromatic polyimides containing ortho-positioned functional groups (e.g., -OH and -SH) (Fig. 1). Two types of changes in chain structure occur during the rearrangement that alter chain packing: (i) random chain conformations resulting from the formation of meta- and para-linked chains (Fig. 1A); and (ii) relatively flexible, twisting pairs of short flat planes (α and β) that convert to single long flat planes (γ) (Fig. 1B) that are much more rigid than those of the parent moieties [e.g., the torsional angle (φ_2) of benzoxazole-phenylene ring is close to 0° at the energy-minimized state because the coplanar conformation is favored due to resonance stabilization]. The use of stiff, rigid chain elements (e.g., benzoxazole-phenylene ring or benzithiazole-phenylene ring) prevents large intrachain, indiscriminant torsional rotation, increases the efficiency of cavity formation, and inhibits rapid collapse of the created cavities. These materials are thermally stable, and the structural rearrangements occurring during this process do not correspond to partial burning (or carbonization) of the underlying polymer structure, a process that has been used in other cases to enhance gas separation properties of polymers.

If managed properly, these changes in chain conformation and topology create well-connected, narrow size distribution free-volume elements (i.e., cavities) appropriate for molecular separations. For example, PALS analysis of a precursor polymer [PIOFG-1, synthesized from 4,4'-(hexafluoroisopropylidene)-diphthalic anhydride (6FDA) and 2,2'-bis(3-amino-4-hydroxylphenyl) hexafluoropropane (bisAPAF) via thermal imidization up to 300°C] and its corresponding thermally rearranged samples (i.e., TR-1-350, TR-1-400, and TR-1-450, respectively) shows that the polymer undergoes microstructural change depending on the extent of rearrangement (*16*). Thermal degradation of the polymer chains is not observed within the heat-treatment temperature ranges, based on results from thermogravimetric analysis coupled with mass spectroscopy (fig. S1A) and elemental analysis (table S2). Spectroscopic analysis (i.e., Fourier transform–infrared) provides convincing evidence that the conversion from imide to benzoxazole is achieved (fig. S1B).

Figure 2 shows that the cavity radius of PIOFG-1 polymer (which is centered at about 0.28 nm and is very broad) increases to ~0.4 nm, and the distribution of cavity sizes becomes narrow as the thermal rearrangement temperature increases to 450°C. PALS analysis reveals an increase in *o*-positronium (*o*-Ps) lifetime as rearrangement temperature increases from 300° to 450°C. In general, longer o-Ps lifetime indicates larger cavity sizes (*17*). The *o*-Ps intensity (%) increases by 700% as thermal rearrangement temperature is increased to 400°C, but decreases above this temperature. Notably, despite increasing *o*-Ps lifetime, the reduction of *o*-Ps intensity in the sample treated at 450°C indicates that an increase in mean cavity size is accompanied by a decrease in the number of cavities, suggesting coalescence of

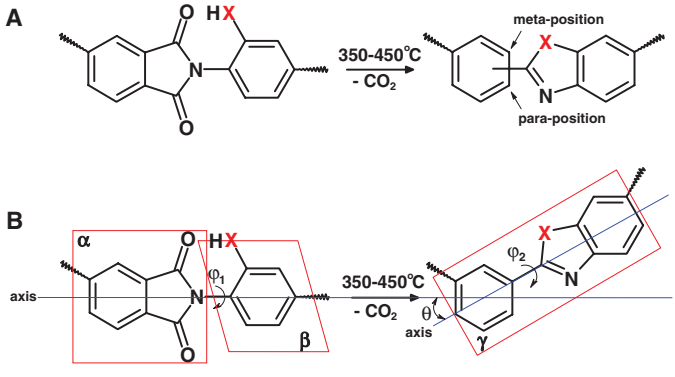

Fig. 1. Two major factors contributing to structural change during thermal chain rearrangement of polyimides containing ortho-positioned functional groups (X is O or S). (**A**) Change of chain conformation—polymer chains consisting of meta- and/or para-linked chain conformations can be created via rearrangement. (**B**) Spatial relocation due to chain rearrangement in confinement, which may lead to the generation of free-volume elements [α plane, phthalic imide ring; β plane, XH-containing phenylene ring; γ plane, newly created phenylene-heterocyclic ring (if X is O, benzoxazole-phenylene ring; if X is S, benzithiazole-phenylene ring); φ_1 and φ_2, dihedral angle; θ, tilting angle after transformation].

[1]School of Chemical Engineering, Hanyang University, Seoul 133-791, Korea. [2]Center for Energy and Environmental Resources and Department of Chemical Engineering, The University of Texas, Austin, TX 78758, USA. [3]The Commonwealth Scientific and Industrial Research Organization (CSIRO) Materials Science and Engineering, Private Bag 33, S Clayton, VIC 3169, Australia. [4]Australian Synchrotron Research Program, Building 434, 9700 South Cass Avenue, Argonne, IL 60439, USA.

*To whom correspondence should be addressed. E-mail: ymlee@hanyang.ac.kr

smaller cavities to form larger ones. Hourglass-shaped cavities, having narrow neck regions separating much larger adjacent chambers, are consistent with this scenario. To have excellent separation properties, the small neck regions must not be too large relative to the size of the molecules being separated, because large openings enable relatively nonselective flow mechanisms (e.g., Knudsen flow) (*7*). However, large cavities adjoining the necks will contribute to high rates of molecular transport. The large cavity size of the fully converted sample (TR-1-450) is smaller than that of PTMSP (0.675 nm) but substantially larger than that of common glassy polymers (e.g., 0.286 nm for polysulfone; 0.289 nm for polycarbonate) (*17*). Similar behavior is observed in other PIOFG samples prepared by a combination of other monomers based on the same methodology.

Synchrotron small-angle x-ray scattering (SAXS) measurements also indicate structural changes over the q-range 0.1 to 0.5 $Å^{-1}$ ($q = 4\pi\sin\theta/\lambda$, where λ is the x-ray wavelength and 2θ is the scattering angle). Specifically, a peak is apparent in the SAXS profiles for samples processed at 400° and 450°C, but not in those processed at lower temperatures (Fig. 2). Furthermore, the peak in the 450°C sample is more pronounced and centered at a lower q than that of the 400°C sample. If we attribute this peak to scattering from cavities, these data suggest that cavities increase in size (i.e., the peak shifts to small q) at higher treatment temperatures.

To explore the separation properties of these polymers (hereafter referred to as TR polymers), we prepared dense membranes (thickness ~20 to 30 μm) for pure and mixed-gas permeability experiments. Figure 3 shows the gas separation performance of several families of polymers considered for CO_2/CH_4 separation at 35°C. Such separations are vital in natural gas processing, landfill gas recovery, and enhanced oil recovery (*18*).

TR polymers demonstrate excellent CO_2/CH_4 separation performance, surpassing the CO_2/CH_4 separation limitation (i.e., the "upper bound" line in Fig. 3A) (*19*) of typical polymer membranes (TR polymers also exceed the separation limit of other notable gas pairs such as O_2/N_2 and H_2/N_2). Counterintuitively, the CO_2 permeability and CO_2/CH_4 selectivity are both high, in contrast to the behavior of conventional strongly size-sieving polymer membranes, where high CO_2/CH_4 selectivity invariably leads to low CO_2 permeability (*20*). On the permeability-selectivity map, the separation performance of our polymer membranes is intermediate between the performance of common polymers and carbon molecular sieve membranes. As revealed by PALS and SAXS, the unusual microstructure of TR polymers (i.e., large cavities) provides an explanation for their high gas permeabilities, and the constriction formed by cavity coalescence is presumably responsible for their precise discrimination among gas molecules such as CO_2 and CH_4. In addition, gas separation results (Fig. 3A) reveal that the cavity size in TR polymers can be tuned by adding small acidic dopants (e.g., HCl and H_3PO_4) because TR polymers include basic nitrogen atoms (-C=N-) on the heterocyclic rings (e.g., benzoxazole ring). After doping, the CO_2 permeability decreases but CO_2/CH_4 selectivity increases. However, after dedoping, the permeability and selectivity return to their original values, indicating that the cavity size and shape can be tailored.

In CO_2/CH_4 separation, CO_2 typically acts as a plasticizer, swelling the polymer matrix, causing the permeation of CH_4 to increase more than that of CO_2, which decreases selectivity (*21*). Glassy polymers such as polyimides and cellulose acetate exhibit substantial decreases in CO_2/CH_4 selectivity in mixed-gas experiments, particularly at high CO_2 fugacity. In contrast, TR polymer membranes do not exhibit substantially reduced selectivity, even at high CO_2 concentration (~80 mol%) and high CO_2 fugacity (~15 atm) (Fig. 3B). The small reduction in selectivity with increasing CO_2 fugacity is caused by a stronger decrease in CO_2 permeability as compared to CH_4 permeability, which is typical for glassy polymer membranes and is due to the effect of competitive sorption in mixtures (*22*, *23*). The CO_2 and CH_4 permeabilities slightly decrease with increasing CO_2 fugacity in all CO_2/CH_4 mixtures (fig. S4), and there is no evidence of plasticization. That is, TR polymer membranes show excellent resistance to plasticization at CO_2 partial pressures as high as 20 atm.

Gas permeabilities of TR polymers are often two orders of magnitude higher than those of the original PIOFG polymers but are still lower than those of PTMSP, the most permeable polymer. However, selectivities for important gas separations (e.g., O_2/N_2 and CO_2/CH_4) are much higher than in PTMSP (*24*) but comparable to or slightly lower than in carbon molecular sieve membranes (*25*). For TR polymers, the order of permeability is $CO_2 > H_2 > He > O_2 > N_2 > CH_4$, similar to that observed in ultrahigh free-volume polymers like PTMSP (*24*).

The outstanding performance results from largely unique cavity formation caused by random chain conformations during thermal molecular rearrangement. A few comparable studies are found in the literature. Barsema *et al*. (*26*) studied commercial polyimide membranes treated at different temperatures (300° to 525°C). They observed that the gas permeability of polyimide membranes treated below the thermal decomposition temperature (<450°C) did not change noticeably, but was slightly reduced due to polymer densification. At the decomposition temperature, the treated membranes exhibited a small increase in gas permeability.

A possible reason why these polymers have unique cavity sizes and shapes might be related to the role played by CO_2 molecules escaping from the original polymer matrix. Therefore, we designed a carboxylic acid group–containing polyimide film and performed the same thermal treatment. Here, the decarboxylation also occurs in a similar temperature range (T = 400° to 500°C). However, no outstanding change in gas permeability was apparent relative to that of the parent polyimide. From our model study, the evolution of CO_2 is not a decisive factor in the formation of gas-accessible free volume or cavities (fig. S5).

The polymers under investigation exhibit pseudo-microporous characteristics that can be probed by nitrogen adsorption/desorption, a technique usually applied to inorganic microporous materials rather than polymers. Conventional dense polymers are "nonporous" in that free-volume elements do not span the sample, so Brunauer-Emmett-Teller (BET) analysis is rarely used to characterize them (*27*). Nitrogen adsorption was used to study two PIOFG polymers [PIOFG-1 and PIOFG-2 (synthesized from 6FDA and 2,5-diamino-1,4-benzenedithiol (DABT)] and their

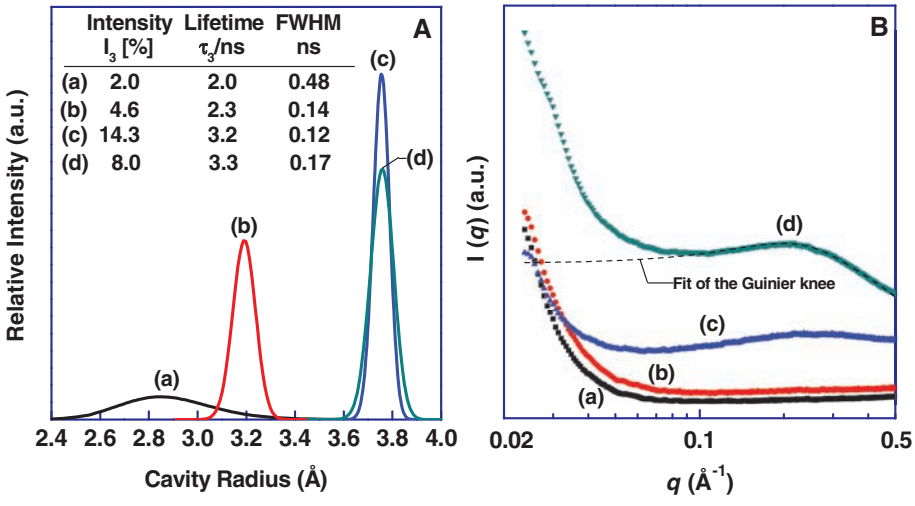

Fig. 2. (**A**) Change of cavity radius (Å) distribution, measured by PALS, of 6FDA + bisAPAF polyimide (PIOFG-1) as a function of thermal treatment temperature. (**B**) SAXS profiles of PIOFG-1 for all four processing temperatures and fit of the Guinier knee of TR-1-450 polymer (black dotted line). (a) PIOFG-1; (b) TR-1-350; (c) TR-1-400; (d) TR-1-450 (FWHM, full width at half maximum from the *o*-Ps lifetime τ_3 distribution).

thermally rearranged analogs at 450°C (TR-1-450 and TR-2-450) (Fig. 4). The PIOFG polymers exhibit an adsorption/desorption isotherm previously observed in glassy polymers (*27*). The nitrogen adsorption/desorption isotherms of TR-1-450 and TR-2-450 are of the irreversible Type I form with hysteresis. The BET surface areas are markedly large for polymers, 510 $m^2\ g^{-1}$ (TR-1-450) and 410 $m^2 g^{-1}$ (TR-2-450), which indicates the presence of substantial amounts of free volume. The hysteresis loops for the TR polymers do not correspond to any of the IUPAC isotherms (*28*), but they are also observed in polymers of intrinsic microporosity (*29*). Materials showing similar isotherms are typically understood to possess "throat and cavity" type microporosity characteristic of activated carbons (*30*). These results further support the hypothesis from PALS of hourglass-shaped cavities.

There are two advantages to the materials described in this work. First, the original polyimides are soluble in common solvents; that is, they can be prepared in the form of hollow fibers and then continuously exposed to heat treatment because these TR polymers produce tough, ductile, robust films rather than brittle, fragile specimens such as zeolite or carbon membranes (table S3). This feature markedly enhances their potential utility and ultimate reduction to practice. Second, it is much easier and simpler to coat these polymers without any defects or cracks onto microporous ceramic support membranes than to coat zeolite, silica, and carbon membranes onto such supports. Recently, we observed that the separation performance of thin-layer coated composite membranes is comparable to that of thick, dense membranes and these membranes do not show permeability decay with time due to physical aging (fig. S5), as do high–free-volume glassy polymer membranes. These polymers with tailored porosity can also be applied as fuel cell membranes. When doped with acid molecules, these polymers exhibit high proton conductivity. For example, the proton conductivity of a H_3PO_4-doped TR-1-450 membrane reaches 0.15 S cm^{-1} at 130°C and low relative humidity (<30%). This value is higher than that of polybenzimidazole (PBI) (<0.1 S cm^{-1} at 200°C) (*31*), the most attractive proton-conducting polymer for high-temperature fuel cells. Currently we believe these polymers sequester water, bound acid, and free acid molecules in the cavity structure, and this phenomenon is responsible for the high conductivity. Most of all, the greatest benefit of these polymers is the ability to tune the cavity size and distribution for specific gas applications by using various templating molecules and heat treatments, with one starting material.

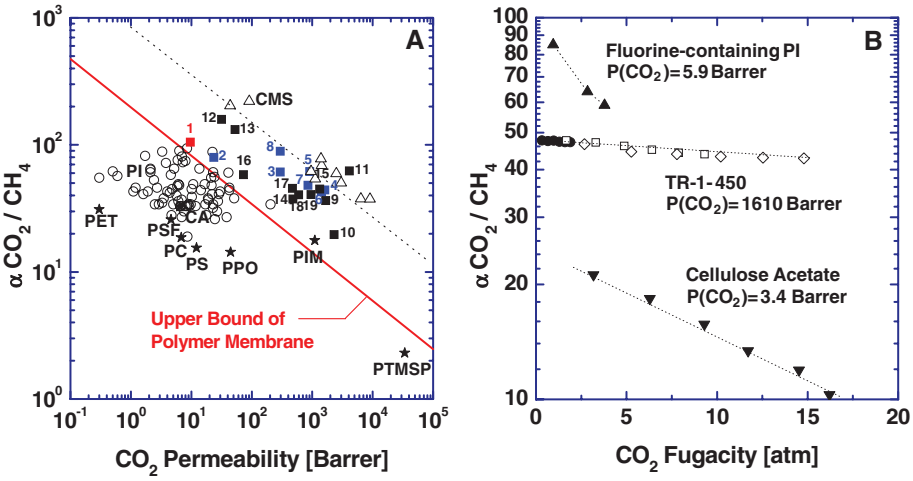

Fig. 3. (**A**) Relation between CO_2 permeability and CO_2/CH_4 selectivity of TR polymers (■) [1, PIOFG-1; 2, TR-1-350; 3, TR-1-400; 4, TR-1-450; 5, HCl-doped TR-1-450; 6, dedoped TR-1-450; 7, HCl-redoped TR-1-450; 8, H_3PO_4-doped TR-1-450; 9 to 19, other TR polymers prepared at 450°C from homopolyimides and copolyimides containing thermally convertible segment units (*16*)]. These data were obtained from pure gas experiments at 35°C. Gas separation performance data of polyimides (PI) reported in the literature (○) (*32*); other polymers (★) (*8*, *29*, *32*) [PET, poly(ethylene terephthalate); PSF, polysulfone; CA, cellulose acetate; PC, polycarbonate; PS, polystyrene; PPO, poly(phenylene oxide); PIM, polymer with intrinsic microporosity; PTMSP, poly(1-trimethylsilyl-1-propyne); CMS, carbon molecular sieve membranes (△) (*6*, *33*)] are included for comparison. The upper bound is from (*19*), and the dotted line is provided to guide the eye. (**B**) Effect of CO_2 partial pressure on mixed-gas CO_2/CH_4 selectivity in TR-1-450 at 35°C. Mixed-gas CO_2/CH_4 feed compositions (in mol% CO_2:mol% CH_4) were 10:90 (●), 50:50 (□), and 80:20 (◇). Mixed-gas data for a fluorine-containing polyimide (*32*) and cellulose acetate (*22*) are included for comparison. The CO_2 permeabilities of fluorine-containing polyimide, cellulose acetate, and TR-1-450 at 35°C and pressure = 10 atm are included for comparison. The dotted lines are provided to guide the eye.

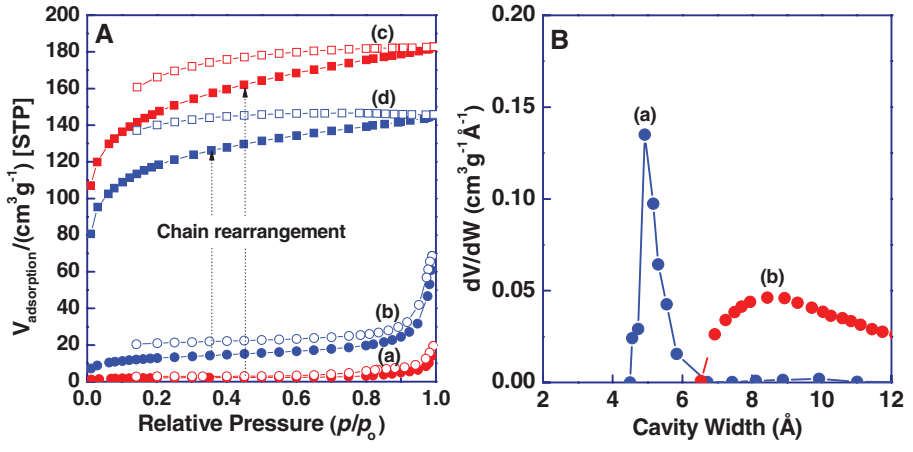

Fig. 4. (**A**) Nitrogen adsorption/desorption isotherms at –195°C for (a) PIOFG-1, (b) PIOFG-2, (c) TR-1-450, and (d) TR-2-450. p/p_0 is the ratio of gas pressure (p) to saturation pressure (p_0), with p_0 = 746 torr. (**B**) Apparent cavity size distributions of (a) TR-1-450, measured by BET, and (b) PTMSP (included for comparison).

References and Notes

1. B. Jeong, Y. H. Bae, D. S. Lee, S. W. Kim, *Nature* **388**, 860 (1997).
2. P. Lightfoot, M. A. Mehta, P. G. Bruce, *Science* **262**, 883 (1993).
3. M. A. Hickner, H. Ghassemi, Y. S. Kim, B. R. Einsla, J. E. McGrath, *Chem. Rev.* **104**, 4587 (2004).
4. H. Lin, E. Van Wagner, B. D. Freeman, L. G. Toy, R. P. Gupta, *Science* **311**, 639 (2006).
5. Z. Lai *et al.*, *Science* **300**, 456 (2003).
6. H. B. Park, Y. M. Lee, *Adv. Mater.* **17**, 477 (2005).
7. Y. Yampolskii, I. Pinnau, B. D. Freeman, *Materials Science of Membranes for Gas and Vapor Separation* (Wiley, London, 2006).
8. K. Nagai, T. Masuda, T. Nakagawa, B. D. Freeman, I. Pinnau, *Prog. Polym. Sci.* **26**, 721 (2001).
9. D. A. Doyle *et al.*, *Science* **280**, 69 (1998).
10. D. Kozono, M. Yasui, L. S. King, P. Agre, *J. Clin. Invest.* **109**, 1395 (2002).
11. I. K. Meier, M. Langsam, H. C. Klotz, *J. Membr. Sci.* **94**, 195 (1994).
12. V. J. Vasudevan, J. E. McGrath, *Macromolecules* **29**, 637 (1996).
13. W. J. Welsh, D. Bhaumik, J. E. Mark, *Macromolecules* **14**, 947 (1981).
14. I. Ye. Kardash, A. N. Pravednikov, *Vysokomol. Soyed.* **B9**, 873 (1967).
15. G. L. Tullos, J. M. Powers, S. J. Jeskey, L. J. Mathias, *Macromolecules* **32**, 3598 (1999).
16. Materials and methods are available as supporting material on *Science* Online.
17. B. R. Wilks *et al.*, *J. Polym. Sci. Part B: Polym. Phys.* **41**, 2185 (2003).
18. H. Lin, E. Van Wagner, R. Raharjo, B. D. Freeman, I. Roman, *Adv. Mater.* **18**, 39 (2006).
19. L. M. Robeson, *J. Membr. Sci.* **62**, 165 (1991).
20. B. D. Freeman, *Macromolecules* **32**, 375 (1999).

21. A. Bos, I. G. M. Pünt, M. Wessling, H. Strathmann, *J. Membr. Sci.* **155**, 67 (1999).
22. T. Visser, N. Masetto, M. Wessling, *J. Membr. Sci.* 10.1016/j.memsci.2007.07.048 (2007).
23. W. R. Vieth, J. M. Howell, J. H. Hsieh, *J. Membr. Sci.* **1**, 177 (1976).
24. I. Pinnau, L. G. Toy, *J. Membr. Sci.* **116**, 199 (1996).
25. H. B. Park, I. Y. Suh, Y. M. Lee, *Chem. Mater.* **14**, 3034 (2002).
26. J. N. Barsema *et al.*, *J. Membr. Sci.* **238**, 93 (2004).
27. O. M. Ilinitch *et al.*, *Micropor. Mesopor. Mat.* **31**, 97 (1999).
28. K. S. W. Sing, R. T. Williams, *Adsorpt. Sci. Technol.* **22**, 773 (2004).
29. P. M. Budd, N. B. McKeown, D. Fritsch, *J. Mater. Chem.* **15**, 1977 (2005).
30. S. J. Gregg, K. S. W. Sing, *Adsorption, Surface Area and Porosity* (Academic Press, London, 1982).
31. J. A. Asensio, P. Gomez-Romero, *Fuel Cells* **5**, 336 (2005).
32. S. A. Stern, H. Kawakami, A. Y. Houde, G. Zhou, U.S. Patent 5,591,250 (1997).
33. K. M. Steel, W. J. Koros, *Carbon* **41**, 253 (2003).
34. This work was supported by the Carbon Dioxide Reduction and Sequestration Center, one of the 21st Century Frontier R&D Programs funded by the Ministry of Science and Technology in Korea. Positron experiments were performed within the framework of the ARC Centers of Excellence program through the Australian Research Council (ARC) Center for Electromaterials Science. CSIRO's Water for a Healthy Country Flagship and the Division of Materials Science and Engineering in CSIRO are acknowledged for their support of the internal membrane research program and this international collaboration. H.B.P. and B.D.F. acknowledge the support of the U.S. Department of Energy (DE-FG03-02ER15362) and the U.S. National Science Foundation (CTS-0515425).

Supporting Online Material
www.sciencemag.org/cgi/content/full/318/5848/254/DC1
Materials and Methods
Figs. S1 to S6
Tables S1 to S3
References

19 June 2007; accepted 7 September 2007
10.1126/science.1146744

Microfluidic Adhesion Induced by Subsurface Microstructures

Abhijit Majumder, Animangsu Ghatak,* Ashutosh Sharma

Natural adhesives in the feet of different arthropods and vertebrates show strong adhesion as well as excellent reusability. Whereas the hierarchical structures on the surface are known to have a substantial effect on adhesion, the role of subsurface structures such as the network of microchannels has not been studied. Inspired by these bioadhesives, we generated elastomeric layers with embedded air- or oil-filled microchannels. These adhesives showed remarkable enhancement of adhesion (~30 times), which results from the crack-arresting properties of the microchannels, together with the surface stresses caused by the capillary force. The importance of the thickness of the adhesive layer, channel diameter, interchannel spacing, and vertical position within the adhesive has been examined for developing an optimal design of this microfluidic adhesive.

The feet of different arthropods and vertebrates show a remarkable ability to attach to almost any surface with varying surface properties and roughness (*1*–*6*). These biological adhesives not only show high adhesive strength, but they can also be detached rapidly and reused over and over. They are self-cleaning and do not leave any marks or footprints after they walk over a surface. Man-made pressure-sensitive adhesives lack these amazing qualities because their high adhesive strength is derived from their viscoelasticity. Although viscous dissipation increases the work or energy of adhesion, the failure occurs at the bulk of the adhesive rather than at the interface, which prevents a clean separation of the adhesive from the surface and also prevents its reusability. Viscoelastic adhesives are also susceptible to fouling by particulate contamination.

The extraordinary ability of naturally occurring adhesives of animals and insects, in particular, is in part related to the complex and hierarchal structural morphologies of their attachment pads (*2*–*8*), which use mechanisms of adhesion other than viscoelasticity (such as, friction, suction, and molecular interactions). Several studies on model textured surfaces (*9*–*14*) have shown that surface patterning can enhance adhesive strength remarkably. This is because the crack propagation is arrested when it encounters a surface discontinuity and has to be reinitiated thereafter. Crack initiation requires much higher stress than does propagation of the crack on a smooth surface (*10*, *11*).

Whereas the previous studies have focused on adhesion as an interfacial phenomenon and have thus employed surface-modified and -textured adhesive layers, we show that air and viscous domains or "patterns" buried within the subsurface or bulk phase can have equally important strong dissipative effects on the work of adhesion and, at the same time, offer a clean reversible separation. We embeded microchannels of different diameters at various vertical and spatial positions within cross-linked elastomeric adhesive layers bonded to a rigid substrate (*15*). A flexible microscope coverslip was then brought into complete contact with this adhesive and lifted vertically from its hanging edge at a constant rate, as shown in Fig. 1A. The flexibility of the adhering coverslip was chosen such that it underwent small bending during peeling. Small bending allows for a precise estimation of the interfacial adhesion strength directly from the force versus displacement measurements. A more general form of the experiment would be to peel an adhesive film bonded to a flexible backing off of another flexible plate. For small bending of the plates, the results for this general geometry are in fact equivalent to the experimental setup employed here by appropriately defining the rigidity of the peeled plate.

The peel experiments (Fig. 1A) on an elastic film (*16*) with air-filled microchannels shows that the contact line between the film and the plate or the crack does not propagate smoothly, but rather with intermittent arrests and initiations at the location of the channels (figs. S1 and S2). Thus, the channels act as a barrier for crack propagation on the surface of the film. This aspect is also captured in the plot of the peeling torque $M = F \cdot a$ against displacement Δ of the flexible plate (Fig. 1B), where a is the distance of the crack from the point of application of the load F. The plot shows the existence of several peaks, the first one corresponding to the formation of the cusp-shaped crack at the edge of the film (*10*, *11*) and the subsequent ones appearing because of the arresting effect of the buried channels. With an increase in Δ, the crack approaches an intermediate channel and remains arrested in its vicinity, whereas F continues to rise. The torque now increases linearly until it reaches a critical value at which the crack nucleates in the form of a cavity at the other side of the channel, and the torque increases sublinearly thereafter. Finally, the torque decreases sharply after a complete opening of the crack and its catastrophic propagation. The average maximum torque, $\overline{M}_{max}$, at which the cracks initiate is plotted in Fig. 1C, which shows that with an increase in the film thickness, $\overline{M}_{max}$ varies nonmonotonically, exhibiting very little influence of the channel for both a thick and a thin film. In essence, when the film thickness approaches the channel diameter, the influence is similar to that of adhesion on a fibriller or patterned surface, whereas for very thick films, adhesion is similar to a smooth surface.

For the films thinner than the one with the maximum torque (~100 μm in Fig. 1C), the channels effectively partition the film into smaller portions, which enhances their compliance and consequent crack blunting, as is also seen in the context of adhesives with surface fibrils (*17*–*19*). To counter this effect of crack blunting, excess energy is required to initiate the crack, which eventually gets dissipated after its propagation. The effect of crack blunting is weaker for thin films but becomes more important with an increase in the film thickness, requiring larger crack-initiation torque. Hence, the maximum crack-initiation torque $\overline{M}_{max}$ increases initially with film thickness h, as shown in Fig. 1C. Beyond a threshold thickness (~100 μm in Fig. 1C), the volume fraction of the channels in the

Department of Chemical Engineering and Department of Science and Technology Unit on Nanoscience, Indian Institute of Technology, Kanpur 208016, India

*To whom correspondence should be addressed. E-mail: aghatak@iitk.ac.in